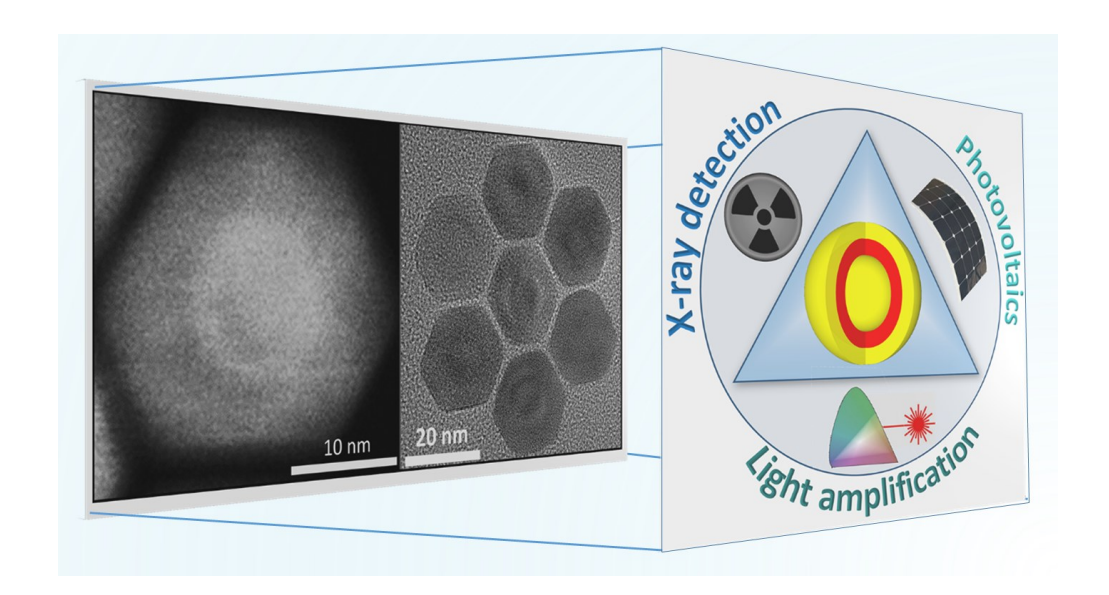
Quantum Shells versus Quantum Dots: Suppressing Auger Recombination in Colloidal Semiconductors.

Jacob Beavon,² Jiamin Huang,^{1,2} Dulanjan Harankahage,^{1,3}, Michael Montemurri,² James Cassidy,^{1,3}, Mikhail Zamkov.^{1,2,*}

The Center for Photochemical Sciences, Department of Physics, and Department of Chemistry, Bowling Green State University, Bowling Green, Ohio 43403

Department of Physics⁴, University of Texas at Dallas, Richardson, TX 75080

Abstract. Colloidal semiconductor nanocrystals (NCs) have attracted a great deal of attention in recent decades. The quantum efficiency of many optoelectronic processes in these nanomaterials, however, declines with increasing optical or electrical excitation intensity. This issue is caused by Auger recombination of multiple excitons, which converts the NC energy into excess heat, whereby reducing the efficiency and lifespan of NC-based devices, including lasers, photodetectors, X-ray scintillators, and high-brightness LEDs. Recently, semiconductor quantum shells (QSs) have emerged as a viable nanoscale architecture for the suppression of Auger decay. The spherical-shell geometry of these nanostructures leads to a significant reduction of Auger decay rates, while exhibiting a near unity photoluminescence quantum yield. Here, we compare the optoelectronic properties of quantum shells against other low-dimensional semiconductors and discuss their emerging opportunities in solid-state lighting and energy-harvesting applications.



INTRODUCTION

Colloidal semiconductor nanocrystals (NCs) have gained significant attention due to their excellent emission characteristics and tunable band gap, which makes them a suitable candidate for a wide range of applications. ¹⁻⁷ Despite a substantial progress in this field, colloidal NCs still face challenges resulting from non-radiative decay due to surface and Auger recombination processes. Surface recombination arises

from the interaction of electron-hole pairs (excitons) with surface charges and, therefore, is potentially manageable through an appropriate treatment of nanoparticle surfaces. Auger recombination, on the other hand, occurs because of the small volume of nanocrystals, which forces multiple excitons to interact non-radiatively. It is a common issue in applications involving intense optical or electrical excitation or high-energy photon detection.⁸⁻¹⁰ For instance, Auger recombination is

identified as the key cause of an efficiency roll-off in high-brightness quantum dot (QD)-LEDs,¹¹ performance reduction in perovskite solar cells,¹² optical gain decay in NC-based light amplification media,^{13,14} ionization of charged excitons in QD solar concentrators,¹⁵ emission quenching in X-ray scintillators,^{16,17} and brightness reduction in single-dot molecular tracking and imaging applications.¹⁸

In comparison to zero-dimensional (OD) quantum dots, semiconductor NCs with one-dimensional (1D) or twodimensional (2D) geometry display a reduced rate of Auger recombination. 19-23 This phenomenon results from a decrease in Auger rates with a growing exciton volume, 24,25 as was demonstrated by improved multi-exciton characteristics of 1D nanorods,¹⁹ 2D nanoplatelets,²⁰⁻²³ and nanostructures with one of the carriers distributed into the bulk (such as giant CdSe/CdS core-shell QDs).²⁶⁻²⁸ A particularly noteworthy example in this regard is a 2D nanoplatelet geometry, such as CdS/CdSe/CdS core-shell or core-crown NPLs,²⁹ where the QY of biexciton emission can reach unity. Such outstanding performance can be attributed to reduced exciton-exciton Coulomb interactions and a relatively fast rate of radiative recombination that outpaces an already slow Auger process. Nonetheless, the attractive interaction between multiple excitons, which is prevalent in 2D nanoplatelets, hampers their ability to utilize the entire volume of the structure. As a result, the rate of both radiative and nonradiative (Auger) interactions of multiple excitons is increased, leading to short multi-exciton lifetimes, typically in sub nanosecond range. This can have a negative effect on optical devices, causing a short-lived optical gain and high thresholds in lasers and electroluminescent devices, as these features benefit multi-exciton lifetimes.30 from longer

We should also note that in addition to NC volume increase, other innovative strategies have been proposed for Auger suppression. For instance, in core-shell semiconductor NCs, ^{27,28} alloying interfaces can decrease the rate of Auger recombination. ³¹ In cesium lead halide perovskite QDs, efficient extraction of excitons to a chromophore ³² or surface modification to decrease the binding energy of excitons ³³ can alleviate fast Auger recombination. In case of 2D transition metal dichalcogenides, such as WS₂ and MoS₂, the decay of multi-exciton Auger can be inhibited by increasing the number of monolayers. ³⁴

Recently, a near-complete suppression of Auger decay was achieved in semiconductor quantum shells (QSs). $^{35-41}$ Similar to nanoplatelets, QSs offer a relaxed carrier confinement in two spatial dimensions but with repulsive rather than attractive interactions between multiple excitons. The repulsion of excitons leads to a smaller carrier overlap and, therefore, reduced rate of Auger recombination. This was recently demonstrated for CdS-CdSe-CdS core-shell-shell QSs, where the biexciton-to-exciton QY ratio, QY_{XX}/QY_X , lied in the 0.60-0.80 range, even approaching unity for large core QSs. 41 The corresponding Auger lifetime for large-core QSs exceeded 100 ns, surpassing that of other NC geometries by an order of magnitude.

This feature article aims to highlight many promising properties of colloidal QSs and discuss emerging opportunities for developing relevant applications in solid-state lighting and energy harvesting. Auger recombination is an obstacle to most applications of low-dimensional semiconductors and the ability to address this issue will likely yield advances across different disciplines. Here, we perform a comparative analysis between QSs and other nanoscale geometries with a particular emphasis on Auger suppression, optical gain media, and thin film conductivity, highlighting the potential benefits QSs in related applications. We also discuss the prospect of developing QSs from non-toxic and abundant semiconductor systems to be deployed in "printable" nanostructured devices.

The Geometry of Quantum Shells.

The geometry of a CdS_{bulk}-CdSe-CdS quantum shell is illustrated in Figure 1a. Similar to Quantum-Dot Quantum-Wells (QDQW), ⁴²⁻⁴⁸ the CdSe quantum-well layer in colloidal QSs is sandwiched between the two CdS "barrier" components, providing a potential energy minimum to photoinduced charges. The relative positions of conduction and valence energies at QS interfaces lead to a strong radial confinement of holes within the CdSe quantum well. Conversely, electrons are more delocalized in the radial direction, which necessitates the presence of a thick CdS barrier - often further protected by a ZnS shell - to avoid coupling with surface states (Figure 1a).

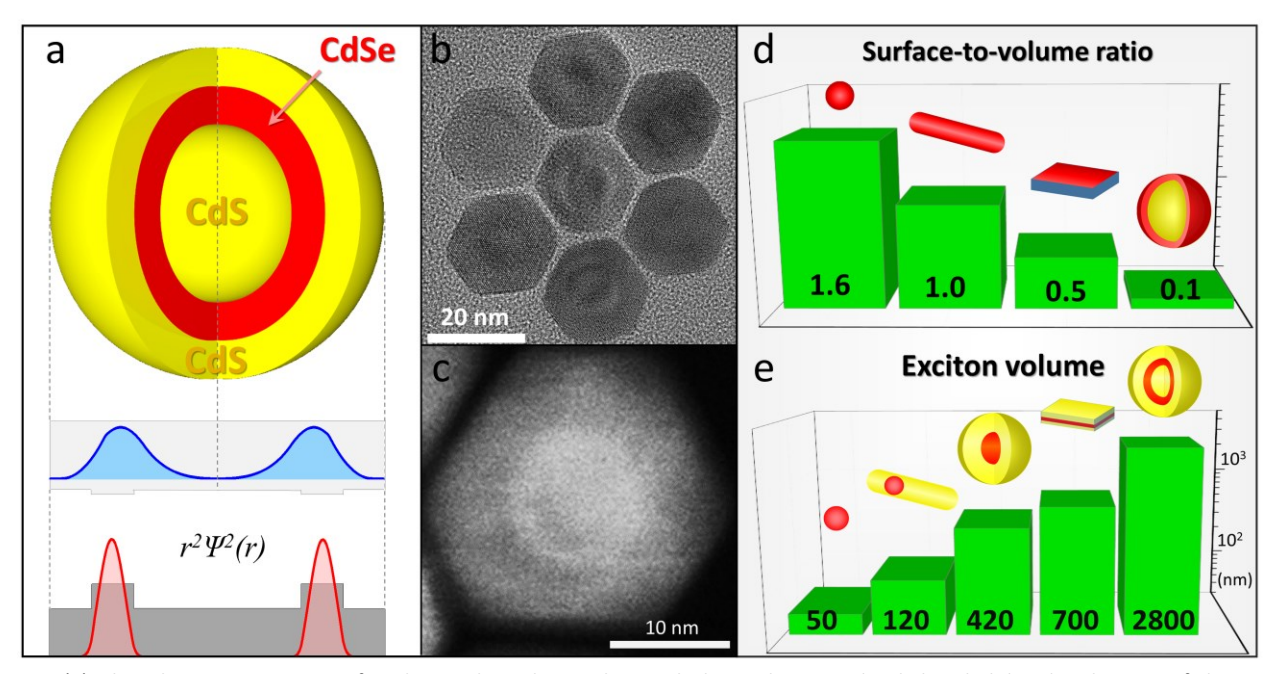


Figure 1. (a). The schematic geometry of a CdS_{bulk}-CdSe-CdS QS. The graph shows theoretical radial probability distributions of electron and hole wave functions in each QS region. (b, c). Characteristic high angle annular dark field (HAADF)-STEM and TEM images of QSs, illustrating the location of the CdSe shell layer. (d,e). A comparison of the surface-to-volume ratios (d) and exciton volumes (e) corresponding to several NC geometries. In (e) - from left to right: 0D CdSe NCs (diameter = 4 nm), CdSe/CdS dot-in-a-rod NCs (dot diameter = 4 nm, rod length = 30 nm), CdSe/CdS core/shell NCs (core radius = 2 nm, shell radius = 10 nm), CdSe/CdS nanosheets (20 nm × 20 nm × 2nm), and CdS_{bulk}-CdSe-CdS QSs (CdSe shell radius = 6 nm, shell thickness = 2 nm, total radius = 10 nm). Panel d,e reprinted from Ref.49 2020 with permission of AIP publishing.

A distinguishing aspect of the quantum shell morphology is a relatively large diameter CdS core domain, which serves as a potential barrier to photoinduced charges. This feature enables the CdSe quantum shell to have one of largest exciton volumes among existing nanocrystal morphologies (Figure 1e). Increasing the volume occupied by multiple excitons diminishes their Coulomb interactions, which, in turn, reduces their Auger recombination rate. Furthermore, the presence of a large core domain in QSs also promotes an increase in the total volume of a nanoparticle. This results in the decreased surface-to-volume ratio of QSs (Figure 1d), which implies a relatively slow rate of carrier surface recombination. Consequently, the two unique features of the QS geometry, large exciton volume and low surface-to-volume ratio, contribute to the suppression of the two main non-radiative decay processes in NCs: Auger and surface recombination.

Synthesis and Optical Properties of Quantum Shells. Recent progress in the synthesis of CdSe-based QSs has been driven by the need to enhance the PL QY as well as to reduce the emission linewidth. It was found that the best practice is to perform the growth of each layer of QSs in a separate reaction,

where the reaction solvent can be optimized for a respective precursor combination. Generally, the first step of the procedure is the synthesis of large-size CdS core nanoparticles (5 – 12 nm in diameter) by means of an aggregative growth strategy.⁵⁰ This approach is based on the coalescence of small-diameter NCs into larger colloids. The key advantage of this method lies in promoting a thermodynamic shape evolution, which naturally leads to particle size focusing with reaction time. In the case of larger nanocrystals, this strategy was more efficient both in terms of reaction speed and product uniformity than a traditional, precursor-based, kinetic growth. In the second step, CdSe layer is grown on the surface of CdS core NCs in a mixture of ODE and dioctylamine. Typically, secondary amines, such as dioctylamine, help reducing the occurrence of post-nucleation during the shell growth, suppressing the formation of isolated CdSe NCs. 51 In the final step, the surface capping layer is deposited over the CdSe shell. This can be achieved with either a thick shell of CdS or a combination of partly alloyed CdS and ZnS shells. Nanoparticles overcoated with a CdS/ZnS composite shell generally show a greater PL QY approaching 90%.52 Meanwhile, QSs dressed with a CdS-only shell layer tend to exhibit a PL QY between 50 and 80% (see Table 1). The deposition of all shell layers during synthesis is generally performed using a slow injection of precursors using two separate syringe pumps.

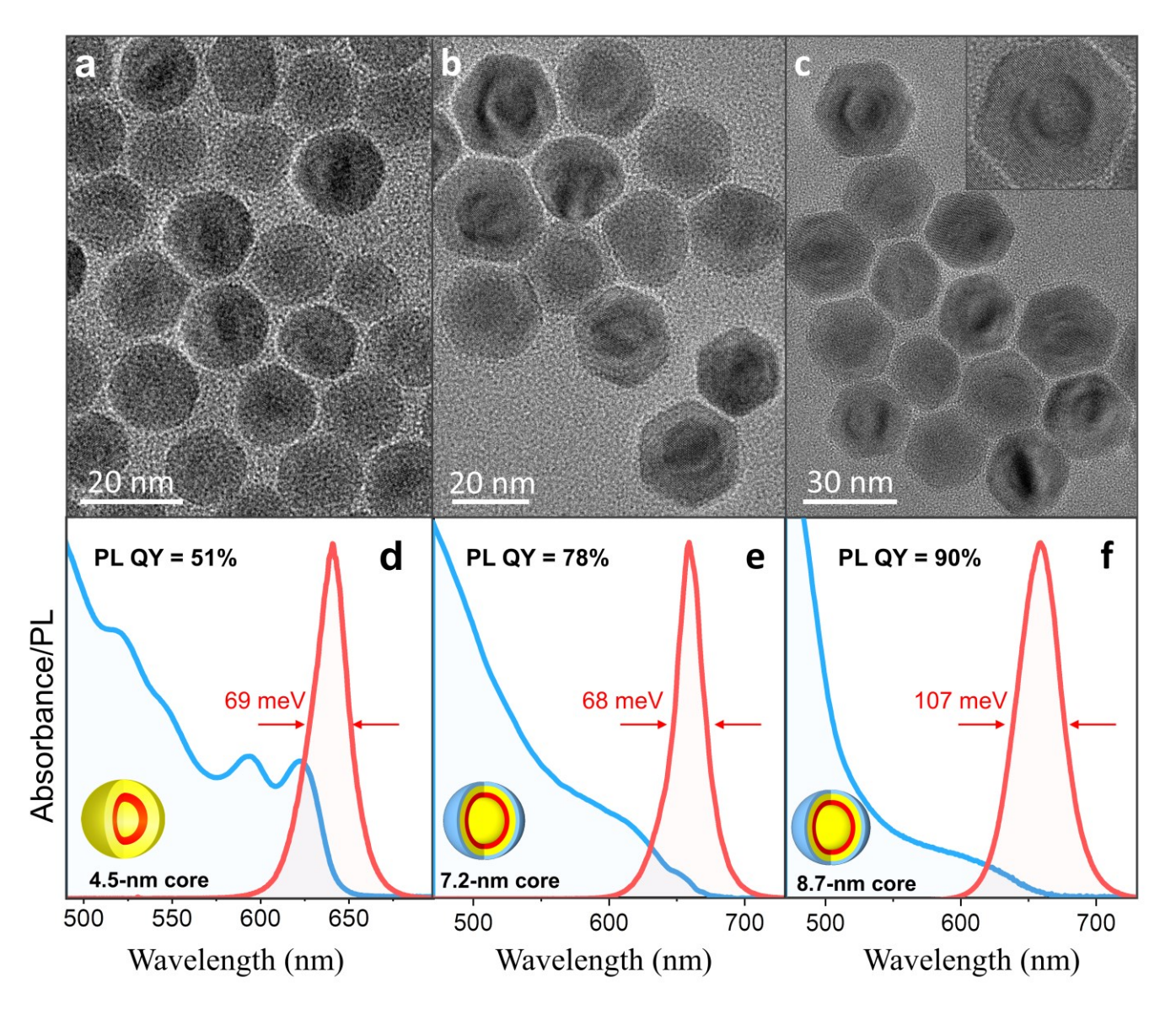


Figure 2. (a-c). Transmission electron microscopy (TEM) images of QSs: (a) -4.5-nm-core CdS_{bulk}-CdSe-CdS QSs, (b) -7.2-nm-core CdS_{bulk}-CdSe-CdS-ZnS QSs, and (c) -9.0-nm-core CdS_{bulk}-CdSe-CdS-ZnS QSs. (d-e). Absorption and emission spectra of QSs: (d) -4.5-nm-core CdS_{bulk}-CdSe-CdS QSs, (e) -7.2-nm-core CdS_{bulk}-CdSe-CdS-ZnS QSs, and (f) -8.7-nm-core CdS_{bulk}-CdSe-CdS-ZnS QSs. Panels a, d adapted with permission from Ref. 38 Copyright 2022 American Chemical Society, Panels c, e, f adapted from Ref. 52.

Figure 2 compares the emission spectra of three quantum shell types: 4.5-nm-core CdS_{bulk}-CdSe-CdS QSs, 7.2-nm-core CdS_{bulk}-CdSe-CdS-ZnS QSs, and 9.0-nm-core CdS_{bulk}-CdSe-CdS-ZnS QSs. The corresponding TEM images are shown in Figures 2a, 2b, and 2c, respectfully. Both 4.5-nm-core and 7.2-nm-core QSs exhibited a narrow emission linewidth of 68-70 meV with a corresponding photoluminescence (PL) quantum yield (QY) of 51% and 78%, respectively. The 8.7-nm-core sample has a broader PL spectrum (linewidth of 107 meV) and a PL QY of 90%.

Generally, it was challenging to achieve a combination of a high PL QY and a narrow PL linewidth, since the former feature requires interfacial alloying that naturally widens the emission peak.

Auger rates and biexciton lifetimes in quantum shells.

From the theoretical standpoint, Auger lifetimes in semiconductor nanocrystals, τ_{Auger} , are expected to grow superlinearly with the nanoparticle volume. Error! Bookmark not

defined.53,54 In the case of QSs exhibiting a comparatively large exciton volume, this can lead to very long τ_{Auger} . In order to explore this hypothesis, we have measured Auger decay times in QSs as a function of the CdSe shell diameter. For these measurements, we followed a standard practice of determining biexciton radiative and non-radiative (Auger) lifetimes from the quantum yield of biexciton emission (QY_{XX}):

$$\tau_{Auger} = 1/k_{Auger} = \frac{QY_{XX}}{\beta k_r (1 - QY_{XX})} \tag{1}$$

$$\tau_{XX} = 1/(k_{Auger} + k_{XX,rad}) = \frac{QY_{XX}}{\beta k_r}$$
 (2)

where k_r is the radiative recombination rate of single excitons, β represents a factor by which biexciton radiative rate is increased

compared to that of single excitons, and k_{Auger} is the Auger recombination rate of biexcitons.

The values of QY_{XX} were determined using fluorescence correlation spectroscopy. To this end, a Hanbury-Brown-Twiss setup, comprising a confocal microscope and a pulsed excitation source, was used to observe antibunching behavior from diffusing nanoparticles in solution. The second-order cross-correlation function, $g^{(2)}(\tau)$, resulting from these measurements has allowed determining the biexciton to exciton QY ratio: $g_{XX} = QY_{XX}/QY_X$. Figure 3a shows the correlation peaks for two types of QSs with corresponding values of g_{xx} ranging from 0.6 to 0.8 (as shown in Table 1). The observed increase in the value of QY_{xx}/QY_X with the size of the QS core was attributed to the suppression of Auger decay in larger-core QSs. Notably, the biexction QY of zero-dimensional CdSe/CdS core/shell QDs is usually lower, with QY_{xx}/QY_X ranging between 10-40%. 55-58

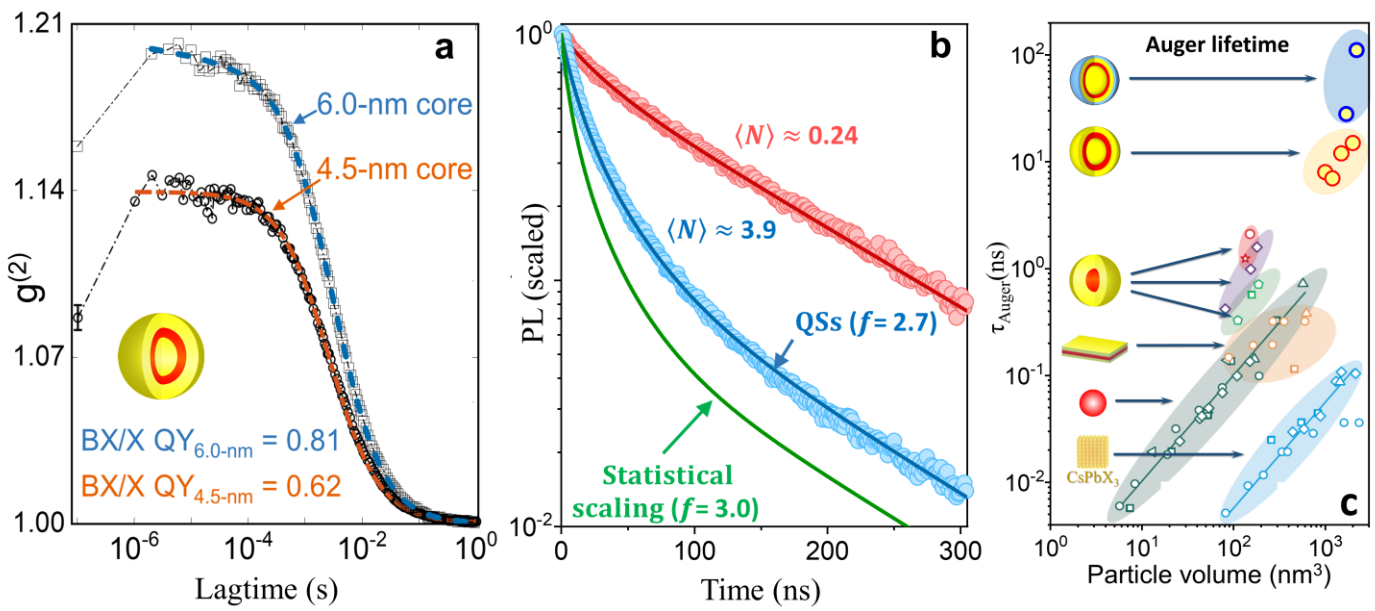


Figure 3. (a). Lagtime dependence of the cross-correlation function, $g^{(2)}$, showing the ratio of biexciton-to-exciton QY (BX/X QY) for 4.5-nm core (orange curve) and 6.0-nm core (blue curve) CdS_{bulk}-CdSe-CdS QSs. (b). PL intensity decay of 8.7-nm-core CdS_{bulk}-CdSe-CdS-ZnS QSs resulting from two excitation regimes: low-power, $\langle N_{eh} \rangle = 0.24$ (red circles) and high-power, $\langle N_{eh} \rangle = 3.9$ (blue circles). The blue curve represents a fit using a parametric model curve. The best fit is obtained using f = 2.7, which deviates from the statistical scaling of multi-exciton rates (f = 3.0, green curve). (c). The dependence of biexciton Auger lifetimes, τ_{Auger} , on particle volume for different types of colloidal nanocrystals. Panel a adapted with permission from Ref. 38 Copyright 2022 American Chemical Society, panel b adapted with permission from Ref. 2. Copyright 2022

The biexciton and Auger lifetimes of QSs can be directly calculated from Eqs. 1 and 2 by using experimental values of g_{xx} and assuming statistical scaling of radiative rates with the number of electron-hole pairs, m (where β = 4), The results of these calculations are summarized in Table 1 and indicate that

the Auger decay in QSs is in fact slow. The corresponding biexciton Auger lifetimes range from 12 to a 110 ns. Notably, these values are at least one order of magnitude greater than those previously reported for CdSe/CdS core-shell QDs, CdS/CdSe/CdS NPLs, or inorganic halide perovskite QDs.²

Table 1. The comparison of multi-exciton characteristics between several morphologies of colloidal quantum shells.

QS Morphology	Core Size (nm)	QY _x	g _{xx}	tau _x (ns)	β	tau _{xx} (ns)	tau _{Auger} (ns)	Ref.
CdS/CdSe/CdS	4.5	0.6	0.62	39	3.3	5.3	10.6	38
CdS/CdSe/CdS	6	0.45	0.81	43	3.3	7.1	16	38
CdS/CdSe/CdS	8.2	0.55	0.88	118	3.3	22.6	61.9	41
CdS/CdSe/CdS/ZnS	7.2	0.8	0.57	84	3.3	13.12	27.09	52
CdS/CdSe/CdS/ZnS	8.7	0.9	0.79	131	3.3	28.35	110.22	52

To obtain a more accurate estimate of biexciton Auger lifetimes in QSs, we adopted a strategy that employs β as a fitting parameter. This approach invokes the power dependence of the ensemble PL with the average number of excitation photons per particle, $\langle N_{eh} \rangle$. Generally, $\langle N_{eh} \rangle$ is calculated as $f \times \sigma$ where f represents the pump fluence and σ is the QS absorption cross-section. For a given value of $\langle N_{eh} \rangle$, the probability of a quantum shall absorbing m photons, f(m), is estimated using the Poisson

distribution: $f(m) = \left\langle N_{eh} \right\rangle^m \times e^{-m} / m!$. Assuming that

Auger recombination of an m-exciton state results in a state with (m-1) excitons, the time dependence of an m-exciton population in a QS, P(m, t), can be determined by solving coupled rate equations:

$$\frac{dP(m,t)}{dt} = k_{m+1}P(m+1,t) - k_m P(m,t)$$
 (2)

where, $k_m = k_{m,r} + k_{m,nr}$, is the total decay rate of an m-exciton state. This model does not take into account charged exciton species (e.g. trions) since their emission is strongly suppressed, as can be inferred from blinking-free trajectories of ZnS-coated QSs (see Figure 4a).

In the case of symmetric multiexcitons, ⁵⁹ decay rates scale statistically with the total number of individual transitions, i.e.

$$k_{m,r} = m^2 k_{r,2}/4$$
, $k_{m,nr} = m^2 (m-1) k_{nr,2}/4$ (3)

However, for spatially asymmetric multi-excitons built from both 1S and 1P states or multiple exciton configurations of large-size nanostructures, the *m*-scaling is expected to deviate from statistical due to a weaker coupling between electron and hole states with different symmetries.⁵⁹ To account for this

difference, we have developed⁵² a universal approach to scaling of multi-exciton radiative and non-radiative decay rates using a variable power parameter f = 2-3, a follows:

$$k_{m,r} = \mathbf{m}^{f-1} k_{r,1}$$
 (4)

$$k_{m,nr} = m^f k_{2,nr}/2^f = \frac{m^f}{2} \times \frac{1 - g_{XX}QY_1}{g_{XX}QY_1} \times k_{1,r}$$
 (5)

The case of f = 3 represents statistical scaling, expected of small-size QDs, and f = 2 mimics the multi-exciton behavior of bulk semiconductors, where Auger recombination rates are significantly lower. The value of f can be obtained by fitting the PL intensity decay. Once the average number of excitons per particle $< N_{eh} >$ is determined, f can then be treated as a single fitting parameter.

Figure 3b illustrates the photoluminescence intensity decay for 8.7-nm-core QSs under two different excitation conditions: low-power ($< N_{eh} > = 0.24$) and high-power ($< N_{eh} > = 3.9$). By fitting a single-parameter model to the experimental PL decay, which is represented by the blue curve in Figure 3b, we find that the best-fit value is f = 2.7. For comparison, we also include the PL decay curve based on statistical scaling of multi-exciton rates (f = 3). By analyzing the experimental data in Figure 3b, we conclude that multi-exciton interactions in QSs deviate from statistical scaling, indicating that the underlying interactions are generally weaker compared to strongly-confined nanocrystal geometries. This deviation may be attributed to a combination of larger QS volume and repulsive interaction between excitons within the QSs. In fact, we propose that in QSs with larger sizes, the carrier density resulting from absorption of multiple photons is

relatively low, which leads to a decrease in Auger decay rates. This unique character of multi-exciton interactions in large-volume QSs has significant implications for the advancement of optoelectronic materials.

Assuming a scaling factor of f = 2.7 for multi-exciton rates in QSs, the corresponding biexciton Auger lifetimes are: $\tau_{2,Auger}$ = 27.4 ns for the 7.2-nm-core and $\tau_{2,Auger}$ = 110.2 ns for 8.7-nm-core QSs (Table 1). Figure 3c compares biexciton Auger lifetimes among various types of 0D-2D colloidal semiconductors. This comparison indicates that QSs have notably longer Auger

lifetimes, which is attributed to their positive binding energy and a large exciton volume.

The extended Auger lifetimes in QSs present significant advantages for prospective applications. First, they facilitate an efficient energy transfer from the biexciton to the exciton state, which is critical for the development of high-brightness LEDs, ionizing radiation scintillators, and other devices operating in a multi-exciton regime. Second, longer multi-exciton Auger lifetimes can help minimize heat generation in nanocrystals, thereby enhancing the durability of optoelectronic devices when subjected to electrical or optical excitation.

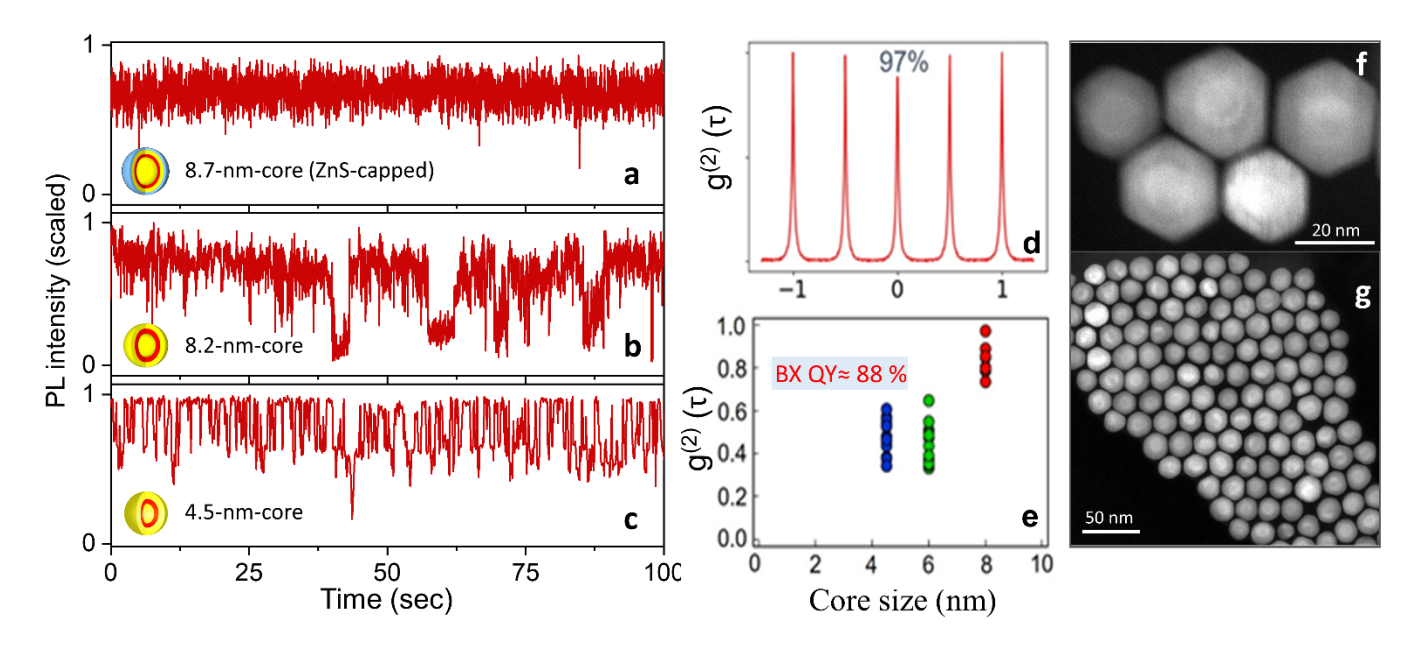


Figure 4. Characteristic PL intensity trajectories of single QSs: (a) - 8.7-nm-core CdS_{bulk} -CdSe-CdS_ZnS QS, (b) - 8.2-nm-core CdS_{bulk} -CdSe-CdS QS, and (c) - 4.5-nm-core CdS_{bulk} -CdSe-CdS QS. (d). An example of a $g^2(\tau)$ function for 8.2-nm-core CdS_{bulk} -CdSe-CdS QSs, showing BX QY of 97%. (e). Statistics of $g^2(\tau)$ values for three types of CdS_{bulk} -CdSe-CdS QSs. (f,g). (HAADF)-STEM images of 8.2-nm-core CdS_{bulk} -CdSe-CdS QSs. Panels (a-c) are adapted with permission from Ref. 52 Copyright 2022 American Chemical Society. Panels (d,e) are adapted with permission from Ref. 41 Copyright 2022 American Chemical Society.

The suppression of Auger recombination in QSs was also evident through profound changes in the PL blinking traces of single particles (Figures 4a-4c). The strange of the usual "on/off" behavior, one could discern distinct intensity levels corresponding to exciton and trion populations. The 4.5-nm-core QSs displayed at least three discrete emission levels, which were identified as neutral exciton (X°), negatively charged (X') trion, and positively charged (X') trion, as shown in Figure 4c. The corresponding PL lifetimes for these populations were determined to be $\tau_X = 45$ ns, $\tau_{X^-} = 17$ ns, and $\tau_{X^+} = 11$ ns, in agreement with ensemble-averaged measurements. In samples with an 8.2-nm core and a CdS-only surface layer, the frequency of "grey" trion states was reduced (Figure 4b). Finally, in the 8.7-nm-core sample with a composite CdS-ZnS surface layer, no

apparent blinking was observed (Figure 4a). This was attributed to the suppressed surface carrier recombination in ZnS-capped QSs.

We have also used single-particle measurements for assessing the biexciton quantum yield, g_{xx} , of CdS_{bulk}-CdSe-CdS QSs with varying core sizes. The g_{xx} was measured using the second-order correlation function, $g^{(2)}(t)$, which confirmed that QS with larger core sizes have relatively higher QY_{xx}/QY_x values. On average, the QY_{xx}/QY_x was found to be 88% on average, with the third quartile exceeding 90%. Notably, some individual QS exhibited QY_{xx}/QY_x values close to 100%, albeit within the measurement error. The distribution plot presented in Figure 4e further reveals that the QY_{xx}/QY_x values are positively correlated with the core

size of QSs, determined from (HAADF)-STEM images (Figures 4f, 4g).

Optical Gain and Lasing Media from Quantum Shells: Benefits of Exciton-Exciton Repulsion.

The suppression of Auger recombination in QSs holds the potential for efficient light amplification in lasing media through the biexciton-gain regime, which requires two excitons per particle. Moreover, QSs have been demonstrated to support a single-exciton optical gain mode, which renders Auger processes inactive. Error! Bookmark not defined. This intriguing phenomenon is

attributed to the splitting of X and XX energy levels, which is caused by the photoinduced electric field of a spatially-separated electron-hole pair of the first exciton. Until now, the phenomenon of exciton-biexciton energy splitting was observed exclusively in type II heterostructured NCs, where electron-hole overlap is relatively small. However, QSs exhibit such X-XX splitting with a type I combination of semiconductors. 61 Additionally, the energy associated with X-XX splitting in QSs, $\Delta_{\rm XX}$ \approx 57 - 63 meV, is notably large.

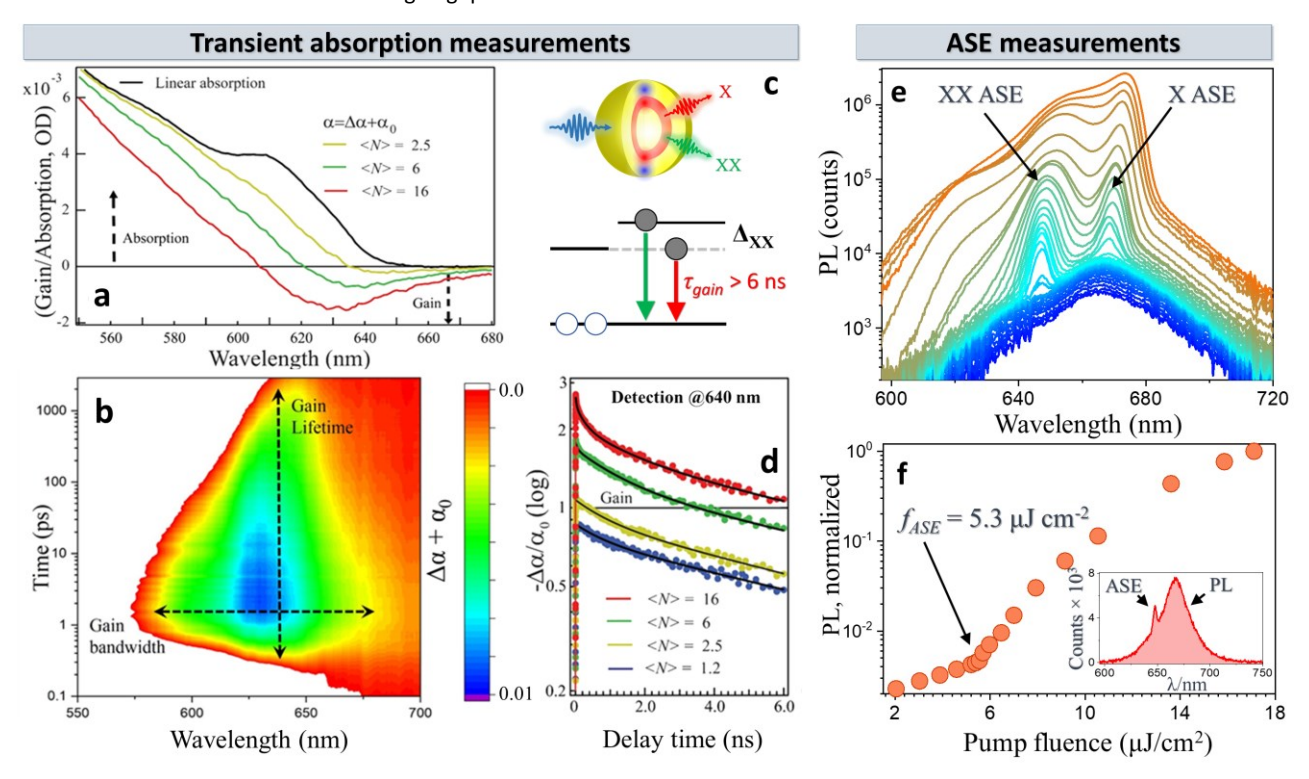


Figure 5. (a) The development of optical gain is demonstrated in the non-linear optical absorption spectra of 4.5-nm-core CdS_{bulk}-CdSe-CdS QSs. Positive values on the left scale indicate absorption, while negative values indicate gain. The black solid line represents a linear absorption spectrum. (b). A contour plot illustrates the lifetime/bandwidth of optical gain in 4.5-nm-core QSs. Positive gain is achieved when the value of $\alpha + \alpha\Delta$ is greater than zero. The pump fluence for this case is 36 μJ/cm². (c). A diagram depicts the impact of repulsion between excitons (X-X) on the absorbing transition energy for the second incoming photon, allowing for single-exciton optical gain in QSs. (d). <N>-dependent TA dynamics illustrating a long-lived optical gain. (e). Emission spectra observed from thin films of 7.2-nm-core QSs for different pump fluences. The narrow ASE peak at ~ 650 nm corresponds to biexciton optical gain, while the onset of a lower-energy feature at around 670 nm, matching the spectral position of the photoluminescence peak, is attributed to a single-exciton gain mechanism. (f). Evolution of the PL intensity for 7.2-nm-core QSs at the spectral position of the biexciton ASE with increasing pump fluence. The corresponding ASE threshold is determined to be 5.3 μJ/cm². The insert demonstrates the onset of biexciton ASE on the high-energy side of the PL peak. Adapted with permission from Ref. 38. Copyright 2022 American Chemical Society. Panels e,f are adapted with permission from Ref. 52. Copyright 2022 American Chemical Society.

In order to analyze the spectral and temporal characteristics of the optical gain in QSs, we conducted femtosecond transient absorption (TA) measurements on dilute nanoparticle solutions. These experiments involve monitoring the absorption change $(\Delta\alpha=\alpha-\alpha_0)$ induced by a femtosecond pump pulse using a white-light continuum probe. Optical gain is realized when $-\Delta\alpha/\alpha_0>1$, where α_0 is a linear absorption.

Figure 5a shows the non-linear absorption spectra for 4.5-nm-core QSs, expressed in terms of number of electron-hole pairs, $\langle N_{eh} \rangle = \phi \, \sigma$, where f is the excitation fluence and $\sigma = 2.3 \times 10^{-13} \, \mathrm{cm^2}$ is single quantum shell's absorption cross-section. (a<0) appears at the single excitation powers, the gain region (a<0) appears at the single exciton (X) transition, matching the spectral position of the PL peak. As the excitation fluence increases, the gain region expands to encompass biexciton transitions at 620 nm (2.02 eV). Such a single-exciton gain mode allowed achieving one of the longest reported optical gain lifetimes among colloidal nanocrystals, $\tau_{gain} > 6 \, \mathrm{ns}$.

Figure 5b displays the bandwidth/lifetime contour plot of the excited state absorption, $\Delta\alpha+\alpha_0$, at excitation fluence of 36 μ J/cm². The optical gain region, $\Delta\alpha+\alpha_0>0$, reveals the gain bandwidth of ~ 300 meV, which is one of the broadest known for colloidal QDs. The realization of a wide amplification range in QSs is attributed to the presence of long-lived high-energy excitons, which are rarely observed in conventional core-shell QDs due to relatively short multiexciton lifetimes.

In order to further investigate the optical gain properties, we have measured the amplified spontaneous emission (ASE) from a spin-coated film of 7.2-nm-core CdS_{bulk} -CdSe-CdS-ZnS QSs (shown in Figure 5e). ⁵² To this end, ultrafast pulses were focused onto a film through a cylindrical lens, resulting in the observation of ASE perpendicular to the excitation direction. The onset of ASE was observed as a spectrally-narrow peak on the higherenergy side of the broader PL band, which exhibited a superlinear dependence on the excitation fluence. The energy difference between the steady-state PL and ASE features suggested a biexciton origin of the optical gain with the corresponding X-X binding energy of 63 meV (exciton-exciton repulsion). Notably, the onset of biexciton ASE in QSs appeared at a relatively low pump fluence of 5.3 μ J/cm² (Figure 5f).

Comparing the exciton-exciton interaction between QSs and 2D nanoplatelets reveals some interesting insights. Both geometries possess large exciton volumes (as shown in Figure 1e), resulting in Auger suppression. However, in 2D NPLs, excitons exhibit an attractive interaction (Δ_{XX} = - 30-45 meV),⁶³ whereas the QS geometry leads to X-X repulsion ($\Delta_{XX} \approx +60$ meV). This difference in exciton-exciton interactions between the two morphologies can be attributed to differences in their respective CdSe quantum well depths. In QSs, the spherical geometry causes electrons to delocalize beyond the quantum well layer, resulting in a positive direct Coulomb coupling (X-X repulsion) Error! Bookmark not defined. Conversely, in NPLs, a stronger lateral confinement compels multiple excitons to form bound "exciton" molecules, leading to a mixture of thermally equilibrated excitons and biexcitons. Both species can contribute to light amplification. It is worth noting that despite such a difference in the character of exciton-exciton interactions, both NPLs and QSs exhibit large enough X-X binding energies to enable optical gain through the Auger-invariant, single-exciton regime.

Photoconductivity and charge transport in quantum shell solids.

The advancement of thin-film QD technologies, including solar cells, photodetectors, and field-effect transistors, relies heavily on achieving efficient electrical conductivity in nanoparticle solids. Consequently, extensive research has been conducted to understand charge transport in nanocrystal assemblies. 64-66 It has been established that nanoparticle grain boundaries play a significant role in impeding charge transfer processes by introducing localized electronic states within the solid.⁶⁷ This is because surface states that exist within the band gap of nanocrystals (such as those observed in Cd chalcogenides) can cause charge trapping and electron-hole recombination. Therefore, assemblies of larger nanocrystals with a lower surface-to-volume ratio generally exhibit improved charge carrier mobility.⁶⁸ The prospect of improving charge transport in thin films by reducing the total surface area of nanoparticles has been frequently explored through the utilization of one- and two-dimensional nanocrystal architectures (e.g. nanotubes,69 nanoplatelets, 70-72 nanorods, 73-75 and atomically coherent superlatices⁷⁶). However, assembling such low-symmetry colloids into close-packed NC films can be challenging and often requires non-trivial processing steps. ⁷⁷

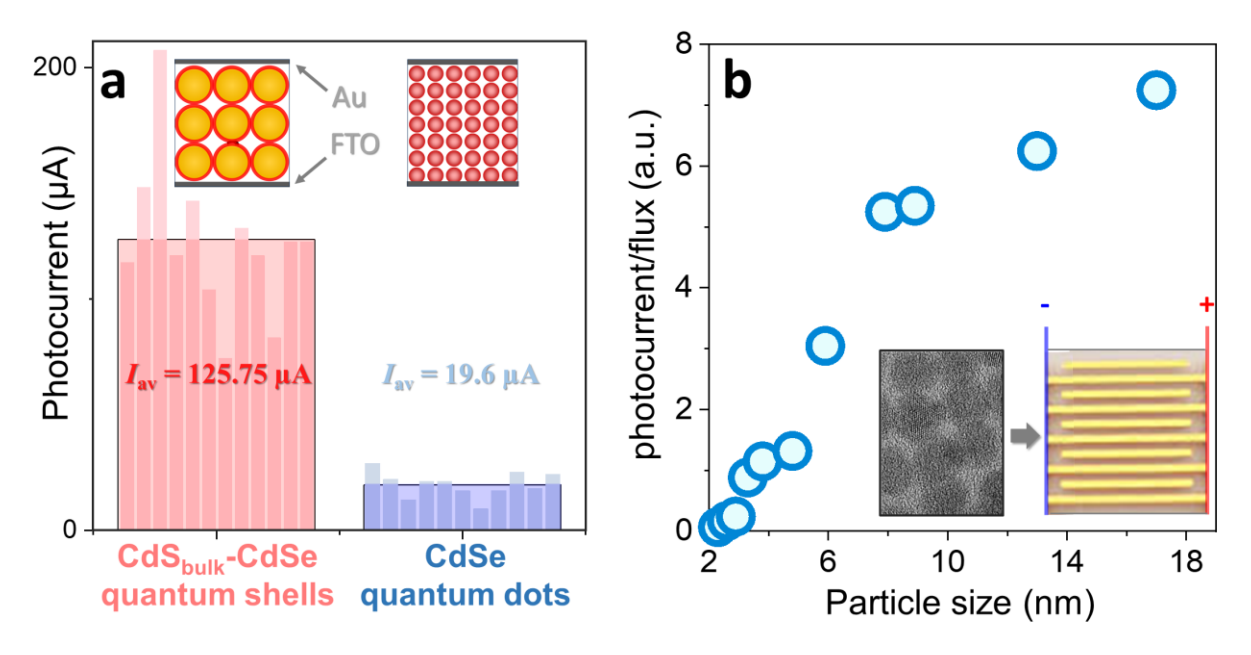


Figure 6. (a). Photocurrent measurements in similarly processed solids of 10.5-nm-core CdS-CdSe QSs (red) and spherical CdSe NCs (blue). Based on averaging of 12 electrode pixels. Adapted with permission from Ref.38 Copyright 2017 American Chemical Society. (b). The flux-corrected photocurrent of close-packed CdSe nanocrystal solids versus the particle size. The insert image shows the substrate used for photoconductivity measurements (10 μm gap, 1mm length, 90 pairs). Adapted with permission from Ref.40 Copyright 2022 American Chemical Society

QSs exhibit one of the lowest surface-to-volume ratios among quantum-confined semiconductors (as shown in Figure 1e) and, consequently, have a smaller fraction of surface atoms. This unique geometry offers potential benefits for charge transport applications, as demonstrated by two recent experiments.³⁵ In one study, spincoated films of 19.6 ± 1.0 nm CdS_{bulk}-CdSe QSs were compared to similarly processed assemblies of 3.9-nm, 0D CdSe NCs. As shown in Figure 6a, the average photocurrent of quantum shell solids was found to be seven times higher than that of CdSe NC films, which was attributed to the reduced interfacial area. Another study⁴⁰ reported the effect of particle size on film photoconductivity. Photocurrent measurements were conducted across nanoparticle solids on substrates with interconnected electrode sets (as shown in Figure 6b, insert), allowing for sampling across different parts of the spin-coated film. Figure 6b demonstrates that increasing the size of CdSe

nanoparticles in the solid resulted in a proportional increase in photoconductivity. For instance, assemblies of 17-nm bulk-sized CdSe nanoparticles exhibited over 100-fold higher conductivity compared to those of 4.5-nm CdSe NCs.

Summary and Outlook

A combination of a large biexciton QY and long biexciton lifetimes in QSs make these nanomaterials an excellent candidate for applications, where Auger recombination is significant. Typically, this refers to materials and devices with more than two charge carriers injected per nanoparticle under optical or electrical excitation, <N>exciton > 1. In the following section, we illustrate several scenarios, where the ability of the quantum shell geometry to suppress Auger decay can enhance the overall quantum efficiency of a process.

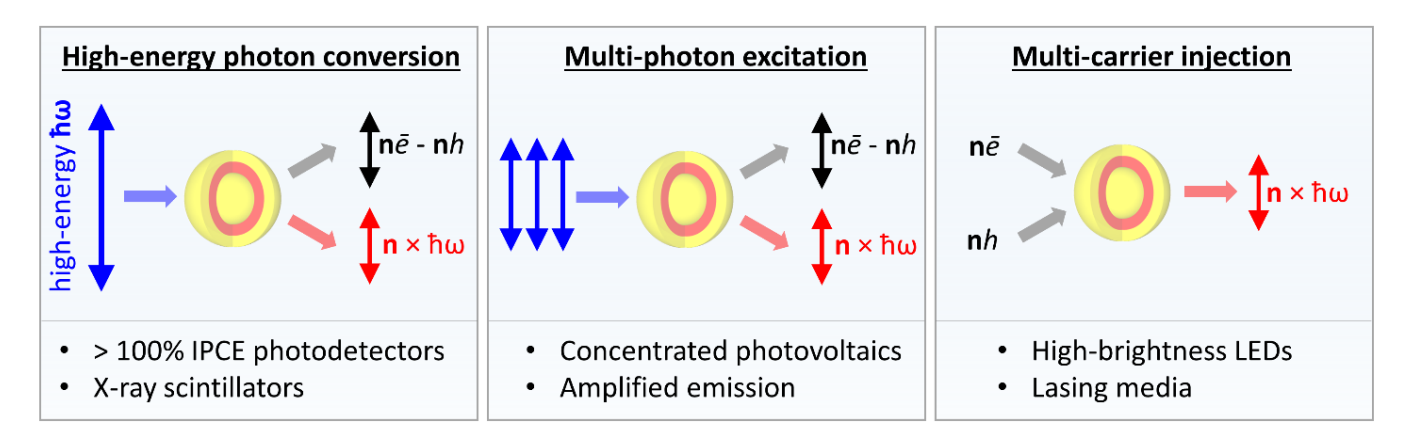


Figure 7. Examples of energy conversion processes, which quantum efficiency is limited by the Auger decay, and can be improved through the use of QSs.

According to Figure 7, there are several processes in nanocrystals, where the Auger recombination is likely to limit the overall quantum efficiency. These include (a) - conversion of high-energy photons into electrical current, (b) - down-conversion of high-energy photons into visible light, (c) - conversion of multiple photons into charge carriers and/or excitons, and (d) - conversion of multiple injected carriers into radiation.

For instance, high-energy photons or concentrated radiation can trigger multiple exciton generation (MEG) in photodetectors and solar cells. 78,79 However, the conversion of this excitation energy in QD-based photovoltaic devices occurs relatively slow through photoinduced charge separation, which typically takes hundreds of picoseconds. 80 As a result, QD materials with short multiexciton Auger lifetimes of less than 100 ps may experience significant efficiency losses in MEG-based applications, such as concentrator photovoltaics.81-83,84 Additionally, fast multiexciton decay is a significant challenge to achieving greater-thanunity external quantum efficiency (EQE) for detecting UV photons, 85,86 which currently has a peak EQE record of 160% (based on PbTe QDs).87 Given their long Auger lifetimes, it is reasonable to expect that QSs could reduce MEG losses in photovoltaic devices and potentially enhance the EQE for UV photon conversion.

The presence of long-lived multi-exciton populations in QSs is also favorable for the development of X-ray scintillators, especially given the growing demand for flexible-substrate, large-area radiation detection.^{88,89} These materials convert highenergy ionizing radiation into visible-range light through a cascade effect (i.e., deexcitation of high-energy charge carriers leading to the formation of band-edge excitons). The resulting

radioluminescence (RL) is a crucial characteristic of a scintillator, as it affects both the detection efficiency and the detection resolution. Despite many advantages of nanoparticle-based scintillators (e.g., ease of processing, high PL QY), ⁹⁰ their RL intensity is limited by fast Auger decay, ¹⁶ as a single X-ray photon can generate tens of excitons, leading to their Auger quenching. For example, recent analysis of CdSe/CdS NPL-based scintillators showed that RL lifetime resulting from 511-keV gamma radiation is comparable to the Auger constant in these materials (approximately 0.5 ns). ⁹¹ Given that the Auger lifetime of QSs is one to two orders of magnitude greater than that of other nanocrystal geometries, the QS morphology may result in improved sensitivity and response timing in scintillators.

Suppressing Auger decay can also have a positive impact on highbrightness LEDs with an output of more than 5,000 cd m⁻².30 Typically, an LED efficiency declines as the current density increases. This process, known as efficiency droop, has been attributed to the Auger decay of charged excitons, or trions. Not only it constrains the achievable brightness levels in daylight display technologies but also causes heat generation, shortening the device lifespan. Recently, it was shown that the suppression of Auger decay in colloidal QDs can extend the trion lifetime to 4-6 ns, leading to virtually droop-free performance with brightness levels of up to 3×10⁵ cd m⁻². 11 Considering that the trion lifetime of QSs is longer (10-30 ns),41 these nanomaterials can become a feasible option for a high-brightness LED technology. The first demonstration of QS LEDs has been recently reported by Malko et al., 41 who has shown that adding a single monolayer of CdS_{bulk}-CdSe-CdS QSs into a CsPbBr₃ perovskite-based LEDs results in a 2.3-fold enhancement of the device EQE. Furthermore, the device incorporating a monolayer of QSs were also shown to triple their brightness to 213 W/m² as compared to perovskite only LEDs.

The demonstrated long-lived optical gain (X⁰ mode) and broad amplification bandwidth (multi-exciton mode) puts QSs on a short list of colloidal semiconductors for optical-gain media applications. One particularly interesting direction, in this regard, is the realization of an electrically-pumped, continuous-wave laser (laser diode), which is the key component of many photonic circuits. Over several decades, the development of laser diodes has predominantly relied on epitaxial quantum wells and epitaxial QDs, which require complex vacuum deposition techniques (e.g., molecular beam epitaxy, chemical vapor deposition). Per Because of the limited robustness of the epitaxial deposition, the development of laser diodes has been lagging behind the expansion of other on-chip components, including detectors, waveguides, and modulators. As a result, quantum shell-based lasers compatible with photonic circuit's applications

could be of potential interest. To expand the spectral range of laser diodes, a Cd-based (CdS-CdSe-CdS) QS "model system" can be replaced with a different combination of semiconductors (see Figure 8).

An area of research in the QS field that has received less attention is their potential for charge-transport applications. QSs have a low surface-to-volume ratio, and thus, a relatively small number of surface atoms, which are often linked to electrical defects. As a result, films of QSs could exhibit improved charge-transport capabilities compared to other nanostructured semiconductors. Although a couple of initial studies have supported this idea, 35,40 there have been no reports of practical applications using QS devices. However, with recent advances in the synthesis of high-quality QSs, this niche can now be explored.

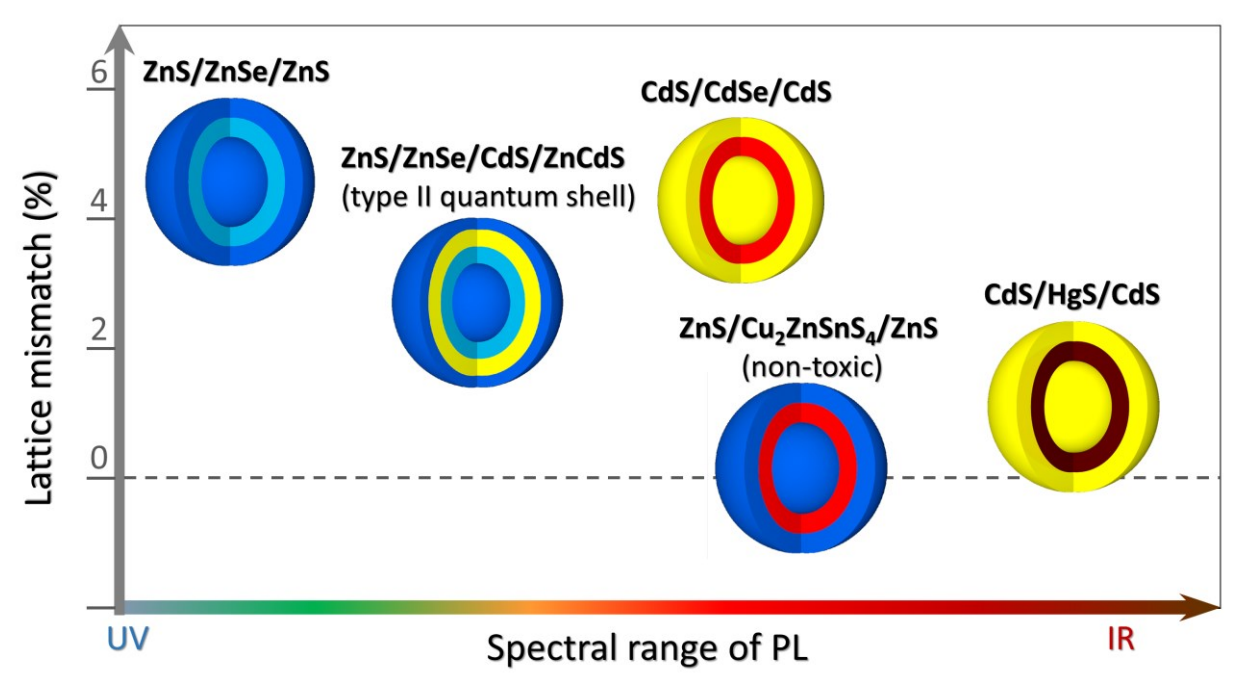


Figure 8. Spectral range of various quantum shell morphologies. The vertical axis represents an average lattice strain of multiple interfaces in the structure. The horizontal axis illustrates an approximate spectral range of emission.

To expand the spectral range of colloidal QSs, CdSe quantum-well layer can be replaced with either blue-emitting ZnSe or IR-emitting HgS. Below, we review several promising QS semiconductor combinations:

<u>ZnS/ZnSe/ZnS</u>. This Cd-free quantum shell morphology can span the blue spectral range of emission (Figure 8). Zn-containing colloidal semiconductors are generally difficult to grow due to Zn oxidation and poor stability of ensuing colloids. However, with recent advances in the chemical treatment of ZnS surfaces,

ZnS/ZnSe/ZnS QSs could ultimately be developed as a promising blue-range emitter.

ZnS/ZnSe/CdS/ZnCdS. This quantum shell geometry is designed to provide a spatial separation between electrons and holes across the ZnSe/CdS interface (type II heterostructure), producing a strong exciton-exciton repulsion effect. This arrangement generates a significant repulsive force between excitons, leading to a pronounced energy difference between X and XX transitions, which is the key to optical gain and single

quantum emitter applications. Notably, due to their type II band alignment, ZnSe/CdS-derived QSs will feature a broadly tunable PL spectral range.⁹⁵

ZnS/CuZnSnS₄/ZnS. This is a non-toxic QS morphology, which is a promising absorber material for PV applications. Because of their small exciton Bohr radius, spherical CuZnSnS₄ nanoparticles usually do not exhibit quantum confinement characteristics. This could change if CuZnSnS₄ is used in a ZnS/CuZnSnS₄ quantum shell geometry since even large-size structures could have some degree of CuZnSnS₄ band gap tuning (via the shell thickness).

<u>CdS/HgS/CdS.</u> This is a promising QS morphology for infrared-range applications. HgS offers a better lattice match to CdS barriers (lattice strain < 1%) than CdSe (> 4%) and provides a stronger confinement to both charge types. A combination of CdSe and HgS layers⁹⁶ can also be used for gradual tuning of the spectral response in the visible-IR range. Meanwhile, the presence of heavy elements, such as Hg, would be beneficial for the potential deployment of QSs in X-ray scintillators.

In general, 2D QSs have the potential to serve as an alternative to existing non-spherical 2D colloids, such as nanosheets and nanoplatelets. QSs offer several advantages, including extended multi-exciton lifetimes, high biexciton quantum yield, singleexciton optical gain that is unaffected by Auger processes, and improved electrical conductivity in solid films. These characteristics play a crucial role in preventing efficiency decline in high-brightness LEDs, photodetectors, and solar cells. Additionally, the unique properties of multi-excitons in QSs hold promise for the development of QD laser diodes, which are essential components of photonic circuits. Meanwhile, the high extinction coefficient of QSs presents new possibilities in the fields of photocatalysis and photochemistry. Ultimately, the architecture of QSs can be expanded to include non-toxic and abundant materials, enabling their utilization in "printable" optoelectronic materials for energy-related applications.

Author Biographies:

Jacob Beavon is a M.S. student in the Department of Physics & Astronomy at Bowling Green State University, currently working under the supervision of Dr. Mikhail Zamkov. He obtained his bachelor's degree from the University of Mount Union in 2021.

Jiaming Huang obtained her B.Sc. in Jiaying University, China in 2011 and continued her MSc at Jinan University where she graduated in 2015. She's currently pursuing her PhD colloidal semiconductor nanomaterials at photochemical sciences center, Bowling Green State University.

Dulanjan Harankahage earned his bachelor's degree from University of Sri Jayewardenepura, Sri Lanka. Afterwards he pursued master's degree at the department of Physics and Astronomy, Bowling Green State University and went on to continue his Ph.D. work in the photochemical sciences center at Bowling Green State University working under the supervision of Dr. Mikhail Zamkov.

Michael Montemurri is a senior college student at Bowling Green State University where he's pursuing a double major in Applied Mathematics and Physics at Bowling Green State University. He's also an undergraduate research assistant working in photovoltaic devices simulations under the supervision of Dr. Marco Nardone as well as synthesizing/characterizing colloidal semiconductor nanomaterials at Zamkov lab.

James Cassidy received his B.A. in chemistry from Saint Anselm College in 2011, and his M.S. in chemistry from the College of William & Mary in 2017 before continuing his education at Bowling Green State university, where he earned his Ph.D. in photochemical sciences. He is currently a postdoctoral fellow in James Frank institute working with Prof. Dimitri Talapin, developing of III-nitride quantum dots.

Prof. Mikhail Zamkov obtained his Ph.D. degrees from Kansas State University in 2003. He is now a Full Professor at Bowling Green State University. His research focuses on the electronic, chemical, and optical properties of semiconductor nanostructures and hybrid nanoscale materials prepared by means of colloidal synthesis. (Web: http://physics.bgsu.edu/~zamkovm/).

Acknowledgment. This work was supported by the Award DE-SC0016872 (MZ) funded by the U.S. Department of Energy, Office of Science. The authors acknowledge the financial support of the University of Michigan College of Engineering and NSF grant #DMR-9871177, and technical support from the Michigan Center for Materials Characterization. JB and MZ acknowledges the support by NSF award #2208834.

References

- ⁴ J. Yang, M. K. Choi, U. J. Yang, S. Y. Kim, Y. S. Kim, J. H. Kim, D.-H. Kim and T. Hyeon, *Nano Lett.*, 2021, **21**, 26–33.
- ⁵ Y. E. Panfil, M. Oded and U. Banin, *Angew. Chem. Int. Ed.*, 2018, **57**, 4274–4295.
- ⁶ F. P. García De Arquer, D. V. Talapin, V. I. Klimov, Y. Arakawa, M. Bayer and E. H. Sargent, Science, 2021, **373**, eaaz8541.
- ⁷ J. Lim, Y.-S. Park and V. I. Klimov, *Nature Mater*, 2018, **17**, 42–49.
- ⁸ U. Banin, M. Bruchez, A. P. Alivisatos, T. Ha, S. Weiss and D. S. Chemla, *The Journal of Chemical* Physics, 1999, **110**, 1195–1201.
- ⁹ V. I. Klimov, A. A. Mikhailovsky, D. W. McBranch, C. A. Leatherdale and M. G. Bawendi, *Science*, 2000, **287**, 1011–1013.
- ¹⁰ V. A. Kharchenko and M. Rosen, *Journal of Luminescence*, 1996, **70**, 158–169.
- ¹¹ J. Lim, Y.-S. Park, K. Wu, H. J. Yun and V. I. Klimov, *Nano Lett.*, 2018, **18**, 6645–6653.
- ¹² J. Chantana, Y. Kawano, T. Nishimura, A. Mavlonov, O. Shen, K. Yoshino, S. Iikubo, S. Hayase and T. Minemoto, Solar Energy, 2021, 217, 342–353.
- ¹³ F. Fan, O. Voznyy, R. P. Sabatini, K. T. Bicanic, M. M. Adachi, J. R. McBride, K. R. Reid, Y.-S. Park, X. Li, A. Jain, R. Quintero-Bermudez, M. Saravanapavanantham, M. Liu, M. Korkusinski, P. Hawrylak, V. I. Klimov, S. J. Rosenthal, S. Hoogland and E. H. Sargent, *Nature*, 2017, **544**, 75–79.
- ¹⁴ V. I. Klimov, A. A. Mikhailovsky, S. Xu, A. Malko, J. A. Hollingsworth, C. A. Leatherdale, H.-J. Eisler and M. G. Bawendi, Science, 2000, 290, 314-317.
- 15 L. A. Padilha, I. Robel, D. C. Lee, P. Nagpal, J. M. Pietryga and V. I. Klimov, ACS Nano, 2011, 5, 5045-5055.
- ¹⁶ Z. Meng, B. Mahler, J. Houel, F. Kulzer, G. Ledoux, A. Vasil'ev and C. Duiardin, *Nanoscale*, 2021, **13**, 19578–19586.

¹ D. A. Hanifi, N. D. Bronstein, B. A. Koscher, Z. Nett, J. K. Swabeck, K. Takano, A. M. Schwartzberg, L. Maserati, K. Vandewal, Y. Van De Burgt, A. Salleo and A. P. Alivisatos, Science, 2019, 363, 1199-1202.

² Y.-S. Park, J. Roh, B. T. Diroll, R. D. Schaller and V. I. Klimov, Nat Rev Mater, 2021, 6, 382–401.

³ Y. Shirasaki, G. J. Supran, M. G. Bawendi and V. Bulović, *Nature Photon*, 2013, 7, 13–23.

¹⁷ J.-X. Wang, X. Wang, J. Yin, L. Gutiérrez-Arzaluz, T. He, C. Chen, Y. Han, Y. Zhang, O. M. Bakr, M. Eddaoudi and O. F. Mohammed, *ACS Energy Lett.*, 2022, **7**, 10–16.

- ¹⁸ F. Pinaud, S. Clarke, A. Sittner and M. Dahan, Nat Methods, 2010, 7, 275–285.
- ¹⁹ Y. Ben-Shahar, J. P. Philbin, F. Scotognella, L. Ganzer, G. Cerullo, E. Rabani and U. Banin, *Nano Lett.*, 2018, 18, 5211–5216.
- ²⁰ C. She, I. Fedin, D. S. Dolzhnikov, A. Demortière, R. D. Schaller, M. Pelton and D. V. Talapin, *Nano Lett.*, 2014, **14**, 2772–2777.
- ²¹ Y. Kelestemur, Y. Shynkarenko, M. Anni, S. Yakunin, M. L. De Giorgi and M. V. Kovalenko, *ACS Nano*, 2019, **13**, 13899–13909.
- ²² B. Guzelturk, M. Pelton, M. Olutas and H. V. Demir, *Nano Lett.*, 2019, **19**, 277–282.
- ²³ B. Chen, S. Chang, D. Li, L. Chen, Y. Wang, T. Chen, B. Zou, H. Zhong and A. L. Rogach, *Chem. Mater.*, 2015, 27, 5949–5956.
- ²⁴ J. P. Philbin and E. Rabani, *Nano Lett.*, 2018, **18**, 7889–7895.
- ²⁵ I. Robel, R. Gresback, U. Kortshagen, R. D. Schaller and V. I. Klimov, *Phys. Rev. Lett.*, 2009, **102**, 177404.
- ²⁶ F. García-Santamaría, Y. Chen, J. Vela, R. D. Schaller, J. A. Hollingsworth and V. I. Klimov, *Nano Lett.*, 2009, **9**, 3482–3488.
- ²⁷ C. H. Lin, E. Lafalce, J. Jung, M. J. Smith, S. T. Malak, S. Aryal, Y. J. Yoon, Y. Zhai, Z. Lin, Z. V. Vardeny and V. V. Tsukruk, *ACS Photonics*, 2016, **3**, 647–658.
- ²⁸ X. Hou, H. Qin and X. Peng, *Nano Lett.*, 2021, **21**, 3871–3878.
- ²⁹ B. T. Diroll, B. Guzelturk, H. Po, C. Dabard, N. Fu, L. Makke, E. Lhuillier and S. Ithurria, *Chem. Rev.*, 2023, **123**, 3543–3624.
- ³⁰ O. V. Kozlov, Y.-S. Park, J. Roh, I. Fedin, T. Nakotte and V. I. Klimov, *Science*, 2019, **365**, 672–675.
- ³¹ G. E. Cragg and A. L. Efros, *Nano Lett.*, 2010, **10**, 313–317.
- ³² J. T. DuBose and P. V. Kamat, *J. Am. Chem. Soc.*, 2021, **143**, 19214–19223.
- ³³ Y. Jiang, M. Cui, S. Li, C. Sun, Y. Huang, J. Wei, L. Zhang, M. Lv, C. Qin, Y. Liu and M. Yuan, *Nat Commun*, 2021, 12, 336.
- ³⁴ L. Yuan and L. Huang, *Nanoscale*, 2015, **7**, 7402–7408.
- ³⁵ N. Razgoniaeva, P. Moroz, M. Yang, D. S. Budkina, H. Eckard, M. Augspurger, D. Khon, A. N. Tarnovsky and M. Zamkov, *J. Am. Chem. Soc.*, 2017, **139**, 7815–7822.

³⁶ N. Kholmicheva, D. S. Budkina, J. Cassidy, D. Porotnikov, D. Harankahage, A. Boddy, M. Galindo, D. Khon, A. N. Tarnovsky and M. Zamkov, *ACS Photonics*, 2019, **6**, 1041–1050.

- ³⁷ G. Nagamine, B. G. Jeong, T. A. C. Ferreira, J. H. Chang, K. Park, D. C. Lee, W. K. Bae and L. A. Padilha, *ACS Photonics*, 2020, **7**, 2252–2264.
- ³⁸ J. Cassidy, B. T. Diroll, N. Mondal, D. B. Berkinsky, K. Zhao, D. Harankahage, D. Porotnikov, R. Gately, D. Khon, A. Proppe, M. G. Bawendi, R. D. Schaller, A. V. Malko and M. Zamkov, *ACS Nano*, 2022, **16**, 3017–3026.
- ³⁹ A. H. Proppe, K. L. K. Lee, C. L. Cortes, M. Saif, D. B. Berkinsky, T. Sverko, W. Sun, J. Cassidy, M. Zamkov, T. Kim, E. Jang, S. K. Gray, B. A. McGuire and M. G. Bawendi, *Phys. Rev. B*, 2022, 106, 045425.
- ⁴⁰ J. Cassidy, D. Harankahage, D. Porotnikov, A. V. Malko and M. Zamkov, *ACS Energy Lett.*, 2022, **7**, 1202–1213.
- ⁴¹A. A. Marder, J. Cassidy, D. Harankahage, J. Beavon, L. Gutiérrez-Arzaluz, O. F. Mohammed, A. Mishra, A. C. Adams, Jason. D. Slinker, Z. Hu, S. Savoy, M. Zamkov and A. V. Malko, *ACS Materials Lett.*, 2023, 1411–1419.
- ⁴² E. P. Pokatilov, V. A. Fonoberov, V. M. Fomin and J. T. Devreese, *Phys. Rev. B*, 2001, **64**, 245329.
- ⁴³ E. A. Dias, J. I. Saari, P. Tyagi and P. Kambhampati, J. Phys. Chem. C, 2012, **116**, 5407–5413
- ⁴⁴ M. Braun, S. Link, C. Burda and M. El-Sayed, *Chemical Physics Letters*, 2002, **361**, 446–452.
- ⁴⁵ J. Xu and M. Xiao, *Appl. Phys. Lett.*, 2005, **87**, 173117.
- ⁴⁶ J. Xu, M. Xiao, D. Battaglia and X. Peng, *Appl. Phys. Lett.*, 2005, **87**, 043107.
- ⁴⁷ D. Battaglia, J. J. Li, Y. Wang and X. Peng, Angew. *Chem. Int. Ed.*, 2003, **42**, 5035–5039.
- ⁴⁸ B. G. Jeong, Y.-S. Park, J. H. Chang, I. Cho, J. K. Kim, H. Kim, K. Char, J. Cho, V. I. Klimov, P. Park, D. C. Lee and W. K. Bae, *ACS Nano*, 2016, **10**, 9297–9305.
- ⁴⁹ J. Cassidy and M. Zamkov, *J. Chem. Phys.*, 2020, **152**, 110902.
- J. Cassidy, D. Harankahage, J. Ojile, D. Porotnikov, L. Walker, M. Montemurri, B. S. L. Narvaez, D. Khon, M. D. E. Forbes and M. Zamkov, *Chem. Mater.*, 2022, 34, 2484–2494.
- ⁵¹ Y. Guo, K. Marchuk, S. Sampat, R. Abraham, N. Fang, A. V. Malko and J. Vela, *J. Phys. Chem. C*, 2012, **116**, 2791–2800.
- ⁵² D. Harankahage, J. Cassidy, J. Beavon, J. Huang, N. Brown, D. Berkinsky, K. Zhang, P. Anzenbacher, R. Schaller, L. Sun, M. Bawendi, A. Malko, B. Diroll, and M. Zamkov, *J. Am. Chem. Soc.*, 2023 (Submitted).

⁵³ J. M. Pietryga, K. K. Zhuravlev, M. Whitehead, V. I. Klimov and R. D. Schaller, *Phys. Rev. Lett.*, 2008, **101**, 217401.

- ⁵⁴ L.-W. Wang, M. Califano, A. Zunger and A. Franceschetti, *Phys. Rev. Lett.*, 2003, **91**, 056404.
- ⁵⁵ A. P. Beyler, T. S. Bischof, J. Cui, I. Coropceanu, D. K. Harris and M. G. Bawendi, *Nano Lett.*, 2014, 14, 6792–6798.
- ⁵⁶ G. Nair, J. Zhao and M. G. Bawendi, *Nano Lett.*, 2011, **11**, 1136–1140.
- ⁵⁷ Y.-S. Park, J. Lim, N. S. Makarov and V. I. Klimov, *Nano Lett.*, 2017, **17**, 5607–5613.
- ⁵⁸ B. D. Mangum, S. Sampat, Y. Ghosh, J. A. Hollingsworth, H. Htoon and A. V. Malko, *Nanoscale*, 2014, **6**, 3712.
- ⁵⁹ V. I. Klimov, J. A. McGuire, R. D. Schaller and V. I. Rupasov, *Phys. Rev. B*, 2008, **77**, 195324.
- ⁶⁰ S. Sampat, N. S. Karan, T. Guo, H. Htoon, J. A. Hollingsworth and A. V. Malko, *ACS Photonics*, 2015, 2, 1505–1512.
- ⁶¹ S. A. Ivanov, J. Nanda, A. Piryatinski, M. Achermann, L. P. Balet, I. V. Bezel, P. O. Anikeeva, S. Tretiak and V. I. Klimov, *J. Phys. Chem. B*, 2004, 108, 10625–10630.
- ⁶² Y.-S. Park, A. V. Malko, J. Vela, Y. Chen, Y. Ghosh, F. García-Santamaría, J. A. Hollingsworth, V. I. Klimov and H. Htoon, *Phys. Rev. Lett.*, 2011, **106**, 187401.
- ⁶³ P. Geiregat, R. Tomar, K. Chen, S. Singh, J. M. Hodgkiss and Z. Hens, *J. Phys. Chem. Lett.*, 2019, **10**, 3637–3644.
- ⁶⁴ C. R. Kagan and C. B. Murray, *Nature Nanotech*, 2015, **10**, 1013–1026.
- ⁶⁵ P. V. Kamat, J. Phys. Chem. C, 2008, **112**, 18737–18753.
- ⁶⁶ N. Y. Morgan, C. A. Leatherdale, M. Drndić, M. V. Jarosz, M. A. Kastner and M. Bawendi, *Phys. Rev. B*, 2002, **66**, 075339.
- ⁶⁷ S. Wieghold, J.-P. Correa-Baena, L. Nienhaus, S. Sun, K. E. Shulenberger, Z. Liu, J. S. Tresback, S. S. Shin, M. G. Bawendi and T. Buonassisi, *ACS Appl. Energy Mater.*, 2018, **1**, 6801–6808.
- ⁶⁸ M. S. Kang, A. Sahu, D. J. Norris and C. D. Frisbie, *Nano Lett.*, 2010, **10**, 3727–3732.
- ⁶⁹ M. F. L. De Volder, S. H. Tawfick, R. H. Baughman and A. J. Hart, *Science*, 2013, **339**, 535–539.
- ⁷⁰ S. Ithurria and B. Dubertret, *J. Am. Chem. Soc.*, 2008, **130**, 16504–16505.
- ⁷¹ S. Ithurria, M. D. Tessier, B. Mahler, R. P. S. M. Lobo, B. Dubertret and Al. L. Efros, *Nature Mater*, 2011, **10**, 936–941.
- ⁷² C. She, I. Fedin, D. S. Dolzhnikov, P. D. Dahlberg, G. S. Engel, R. D. Schaller and D. V. Talapin, *ACS Nano*, 2015, 9, 9475–9485.

⁷³ G. Jia, A. Sitt, G. B. Hitin, I. Hadar, Y. Bekenstein, Y. Amit, I. Popov and U. Banin, *Nature Mater*, 2014, **13**, 301–307.

- ⁷⁴ L. Carbone, C. Nobile, M. De Giorgi, F. D. Sala, G. Morello, P. Pompa, M. Hytch, E. Snoeck, A. Fiore, I. R. Franchini, M. Nadasan, A. F. Silvestre, L. Chiodo, S. Kudera, R. Cingolani, R. Krahne and L. Manna, *Nano Lett.*, 2007, 7, 2942–2950.
- ⁷⁵ N. N. Hewa-Kasakarage, M. Kirsanova, A. Nemchinov, N. Schmall, P. Z. El-Khoury, A. N. Tarnovsky and M. Zamkov, *J. Am. Chem. Soc.*, 2009, 131, 1328–1334.
- ⁷⁶ K. Whitham, J. Yang, B. H. Savitzky, L. F. Kourkoutis, F. Wise and T. Hanrath, *Nature Mater*, 2016, **15**, 557–563.
- ⁷⁷ K. Ariga, M. Li, Gary J. Richards and Jonathan P. Hill, *j nanosci nanotechnol*, 2011, **11**, 1–13.
- ⁷⁸ V. Sukhovatkin, S. Hinds, L. Brzozowski and E. H. Sargent, *Science*, 2009, **324**, 1542–1544.
- ⁷⁹O. E. Semonin, J. M. Luther, S. Choi, H.-Y. Chen, J. Gao, A. J. Nozik and M. C. Beard, *Science*, 2011, 334, 1530–1533.
- ⁸⁰N. Kholmicheva, P. Moroz, E. Bastola, N. Razgoniaeva, J. Bocanegra, M. Shaughnessy, Z. Porach, D. Khon and M. Zamkov, ACS Nano, 2015, 9, 2926–2937.
- 81 G. Nair, L.-Y. Chang, S. M. Geyer and M. G. Bawendi, Nano Lett., 2011, 11, 2145-2151.
- 82 P. V. Kamat, J. Phys. Chem. Lett., 2013, 4, 908–918.
- 83 M. C. Beard, J. Phys. Chem. Lett., 2011, 2, 1282–1288.
- ⁸⁴ A. G. Midgett, J. M. Luther, J. T. Stewart, D. K. Smith, L. A. Padilha, V. I. Klimov, A. J. Nozik and M. C. Beard, *Nano Lett.*, 2013, **13**, 3078–3085.
- 85 C. R. Kagan, E. Lifshitz, E. H. Sargent and D. V. Talapin, Science, 2016, 353, aac5523.
- ⁸⁶ M. V. Kovalenko, L. Manna, A. Cabot, Z. Hens, D. V. Talapin, C. R. Kagan, V. I. Klimov, A. L. Rogach, P. Reiss, D. J. Milliron, P. Guyot-Sionnnest, G. Konstantatos, W. J. Parak, T. Hyeon, B. A. Korgel, C. B. Murray and W. Heiss, *ACS Nano*, 2015, 9, 1012–1057.
- ⁸⁷ H. Goodwin, T. C. Jellicoe, N. J. L. K. Davis and M. L. Böhm, *Nanophotonics*, 2018, 7, 111–126.
- ⁸⁸ L. Clinckemalie, D. Valli, M. B. J. Roeffaers, J. Hofkens, B. Pradhan and E. Debroye, ACS Energy Lett., 2021, 6, 1290–1314.
- ⁸⁹ Q. Chen, J. Wu, X. Ou, B. Huang, J. Almutlaq, A. A. Zhumekenov, X. Guan, S. Han, L. Liang, Z. Yi, J. Li, X. Xie, Y. Wang, Y. Li, D. Fan, D. B. L. Teh, A. H. All, O. F. Mohammed, O. M. Bakr, T. Wu, M. Bettinelli, H. Yang, W. Huang and X. Liu, *Nature*, 2018, 561, 88–93.

⁹⁰ L. A. Padilha, W. K. Bae, V. I. Klimov, J. M. Pietryga and R. D. Schaller, *Nano Lett.*, 2013, **13**, 925–932.

- ⁹¹ R. M. Turtos, S. Gundacker, S. Omelkov, B. Mahler, A. H. Khan, J. Saaring, Z. Meng, A. Vasil'ev, C. Dujardin, M. Kirm, I. Moreels, E. Auffray and P. Lecoq, *npj 2D Mater Appl*, 2019, 3, 37.
- 92 N. Holonyak, R. Kolbas, R. Dupuis and P. Dapkus, IEEE J. Quantum Electron., 1980, 16, 170-186.
- ⁹³ L. A. Coldren, S. W. Corzine and M. L. Mašanović, *Diode Lasers and Photonic Integrated Circuits: Coldren/Diode Lasers 2E*, John Wiley & Sons, Inc., Hoboken, NJ, USA, 2012.
- ⁹⁴ S. Chen, W. Li, J. Wu, Q. Jiang, M. Tang, S. Shutts, S. N. Elliott, A. Sobiesierski, A. J. Seeds, I. Ross, P. M. Smowton and H. Liu, *Nature Photon*, 2016, 10, 307–311.
- ⁹⁵ A. Nemchinov, M. Kirsanova, N. N. Hewa-Kasakarage and M. Zamkov, *J. Phys. Chem. C*, 2008, **112**, 9301–9307.
- ⁹⁶ V. Sayevich, Z. L. Robinson, Y. Kim, O. V. Kozlov, H. Jung, T. Nakotte, Y.-S. Park and V. I. Klimov, Nat. Nanotechnol., 2021, 16, 673–679.